NISS

Arctic sea ice variability: Model sensitivities and a multidecadal simulation

William L. Chapman, William J. Welch,
Kenneth P. Bowman, Jerome Sacks,
and John E. Walsh

Technical Report Number 2
June, 1993

National Institute of Statistical Sciences
19 T. W. Alexander Drive
PO Box 14006
Research Triangle Park, NC 27709-4006
www.niss.org

Arctic sea ice variability:
Model sensitivities and a multidecadal simulation

William L. Chapman[1], William J. Welch[2], Kenneth P. Bowman[1], Jerome Sacks[3], and John E. Walsh[1]

June 1993

---

1 Department of Atmospheric Sciences, University of Illinois, 105 S. Gregory Ave., Urbana, IL 61801
2 Department of Statistics and Actuarial Science, University of Waterloo, Waterloo, Ontario N2L 3G1 Canada
3 National Institute of Statistical Sciences, Research Triangle Park, NC 27709

ABSTRACT

A dynamic-thermodynamic sea ice model is used to illustrate a sensitivity evaluation strategy in which a statistical model is fit to the output of the ice model. The statistical model response, evaluated in terms of certain metrics or integrated features of the ice model output, is a function of a selected set of d (= 13) prescribed parameters of the ice model and is therefore equivalent to a d–dimensional surface. The d parameters of the ice model are varied simultaneously in the sensitivity tests. The strongest sensitivities arise from the minimum lead fraction, the sensible heat exchange coefficient, and the atmospheric and oceanic drag coefficients. The statistical model shows that the interdependencies among these sensitivities are strong and physically plausible. A multidecadal simulation of arctic sea ice is made using atmospheric forcing fields from 1960–1988 and parametric values from the approximate mid-points of the ranges sampled in the sensitivity tests. This simulation produces interannual variations consistent with submarine-derived data on ice thickness from 1976 and 1987, and with ice-extent variations obtained from satellite passive microwave data. The ice model results indicate that (1) interannual variability is a major contributor to the differences of ice thickness and extent observed over timescales of a decade or less, and (2) the timescales of ice thickness anomalies are much longer than those of ice-covered area. However, the simulated variations of ice coverage have less than 50% of their variance in common with observational data, and the temporal correlations between simulated and observed anomalies of ice coverage vary strongly with longitude.

1. Introduction

Over the past few decades, models have become increasingly useful tools in the study of sea ice and the high-latitude climate system. Among the advantages offered by sea ice models are (1) information on variables (e.g., ice thickness, ice strength) that are difficult to measure, (2) the facilitation of diagnostic analyses of the physical and dynamical mechanisms underlying simulated changes of sea ice, and (3) the potential for coupling to atmospheric and oceanic models for simulations of interactions with other key components of the climate system. A primary disadvantage of sea ice models is that their formulation generally involves various algorithms that introduce a host of parametric sensitivities. Because these sensitivities and their interdependencies are often difficult to evaluate in a comprehensive manner, they are rarely documented thoroughly despite the fact that many of the parameters are potentially powerful "tuning knobs" in the sea ice simulations.

The present paper has two components. First, we use a dynamic-thermodynamic sea ice model to illustrate a new procedure for the evaluation of multivariate parametric sensitivities. This procedure provides a means to address the interdependencies of the sea ice model sensitivities. Second, we illustrate advantage (1) above by using the same model, forced by analyzed fields of atmospheric variables, to generate a proxy record of sea ice thickness in the Arctic Ocean. This simulation spans the past few decades, a period for which the few available thickness measurements need spatial and temporal perspective.

2. Sea Ice Model

The model contains Hibler's (1979) two-level dynamic formulation and Parkinson and Washington's (1979) thermodynamic formulation, together with subsequent modifications described by Walsh and Zwally (1990). The model has served as the basis of prior model studies (Ross and Walsh, 1987; Preller and Posey, 1989; Riedlinger and Preller, 1991). While the

formulation has been presented in the earlier papers, we summarize the key elements of the formulation here in order to highlight the parameters that are varied in the sensitivity analysis.

The dynamic formulation is based on a momentum balance for a mass m of ice within a grid cell:

$$m \frac{d\vec{V}_i}{dt} = \vec{\tau}_a + \vec{\tau}_w + m f \hat{k} \times \vec{V}_i - m g \vec{\nabla} H + \vec{F} \tag{1}$$

where $\vec{V}_i$ is the ice velocity; $\vec{\tau}_a$ and $\vec{\tau}_w$ are the wind and ocean stresses on the top and bottom surfaces of the ice; $m f \hat{k} \times \vec{V}_i$ is the Coriolis force (f is the Coriolis parameter); $m g \vec{\nabla} H$ gives the acceleration due to sea surface tilt (H is the dynamic height of the ocean); and $\vec{F}$ is the internal ice stress term. The air and water stresses are computed using prescribed drag coefficients (C_a and C_w) and constant turning angles (ϕ and θ):

$$\vec{\tau}_a = \rho_a C_a \left| \vec{V}_a \right| \left(\vec{V}_a \cos\phi + \hat{k} \times \vec{V}_a \sin\phi \right) \tag{2}$$

$$\vec{\tau}_w = \rho_w C_w \left| \vec{V}_w - \vec{V}_i \right| \left(\left[\vec{V}_w - \vec{V}_i \right] \cos\theta + \hat{k} \times \left[\vec{V}_w - \vec{V}_i \right] \sin\theta \right) \tag{3}$$

where ρ_a and ρ_w are the densities of air and water, $\vec{V}_a$ is the geostrophic wind, $\vec{V}_w$ is the geostrophic ocean current, and $\hat{k}$ is the vertical unit vector. The internal ice stress is evaluated with the aid of a viscous-plastic constitutive law, which relates the ice stress to the ice deformation rate and the ice strength. The ice strength, P, is a function of the grid-cell mean ice thickness, h, and the compactness, A:

$$P = P^* h \exp[-C (1-A)] \tag{4}$$

where P^* and C ($\equiv 20$) are prescribed constants.

The ice thickness and compactness change in response to advection, convergence or divergence, thermodynamic growth or melt, and small numerical diffusion terms included for numerical stability. A key parameter in the treatment of the compactness is a prescribed minimum lead fraction, MLF = 1 - A_{max}, which limits the compactness to A_{max}. The minimum lead fraction permits the inclusion of the effect of small-scale motions within a grid cell, since these motions

tend to maintain a small fraction (several percent) of open water or very thin ice within the pack even during winter. The small areas of open water and thin ice are extremely important to the surface mass, energy and moisture budgets because most of the ocean-atmosphere exchanges of sensible and latent heat occur in these regions, as does much of the new ice growth and salt rejection.

The model's thermodynamic component, which provides the rates of ice growth and melt, has at its core a surface energy budget:

$$(1-\alpha)F_s + F_\ell + D_1\left|\vec{V}_a\right|(T_a - T_o) + D_2\left|\vec{V}_a\right|(q_a + q_o) - \varepsilon\sigma T_o^4 + \frac{K}{h}(T_w - T_o) = 0, \quad (5)$$

where α is the surface albedo, F_s is the flux of solar radiation reaching the surface, F_ℓ is the downcoming flux of longwave radiation, D_1 and D_2 are bulk transfer coefficients for sensible and latent heat, T_a is the air temperature, T_o is the ice (surface) temperature, T_w is the ocean mixed layer temperature, ε is the surface emissivity, σ the Stefan-Boltzmann constant, and K is the thermal conductivity. Given the radiative fluxes (F_s, F_ℓ) and the relative humidity (for q_a), (5) is solved for the surface temperature, T_o. If T_o exceeds the freezing temperature when ice is present, T_o is set to the freezing temperature and the excess energy is used to melt ice. At the bottom surface of the ice, the rate of ice growth or melt is determined by the imbalance between the conduction of heat into the ice and the prescribed vertical flux, F_o, of oceanic heat into the mixed layer.

The downcoming fluxes of solar and longwave radiation are both parameterized in terms of prescribed cloud fractions, C_f, varying from 0.5 in winter to 0.9 in summer. The shortwave flux reaching the surface is the daily integral of Zillman's (1972) expression:

$$F_s = \frac{S\cos^2 Z}{(\cos Z + 2.7)(10^5\, e) + 1.08\cos Z + 0.10}\left(1 - 0.6\, C_f^{\beta}\right) \quad (6)$$

where S is the solar constant, Z is the solar zenith angle, e is the vapor pressure, and β is a prescribed constant. The downcoming longwave flux reaching the surface is obtained from Idso and Jackson's (1969) clear-sky parameterization and an additional contribution proportional to C_f (Parkinson and Washington, 1979):

$$F_\ell = \sigma T_a^4 \left\{1.0 - 0.261 \exp\left[0.00078 (273 - T_a)^2\right]\right\} (1 + \gamma C_f) \quad (7)$$

where γ is a prescribed constant. The sensitivity analysis described in Section 3 includes systematic variations of the parameters β (over the range 1.0–4.0) and γ (over the range 0.1–0.5).

The thermodynamic model includes snowfall at prescribed rates that vary seasonally. In the sensitivity experiments of Section 3, the prescribed snowfall rates are varied systematically so that the annual totals span the range 0–5.0 m yr $^{-1}$. Snow on top of the ice affects the model in two ways. First, the snow serves as an insulator of the ice through the modification of the conductivity K in (5). Computationally, K is a depth-weighted mean of the conductivities of snow and ice. Second, snow has a substantial effect on the absorption of solar radiation through the increase of the surface albedo from approximately 0.60 to 0.80. In the sensitivity experiments, the albedo of snow (α_s) is varied systematically from 0.50 to 1.00, while the albedo of snow-free ice (α_i) is varied from 0.30 to 0.80. By contrast, the albedo of the open water fraction of a grid cell (α_w) is typically about 0.10; the range of values spanned by the experiments described here is 0.00–0.50.

The version of the model used here includes the concentrations and thicknesses of two ice types: multiyear and first-year. Multiyear ice is, by definition, ice that has survived a summer melt season. Both types of ice are advected, diffused and subjected to changes of thickness at rates obtained from separate applications of the surface energy budget in (5). Walsh and Zwally (1990) describe the modifications of the formulation entailed by the distinction of the two ice types.

The model is run with a daily timestep on a 110 km polar stereographic grid (Figure 1). The forcing consists of corresponding daily grids of surface winds and air temperatures. The winds are derived from the sea level pressure analyses archived at the National Center for Atmospheric Research; from 1979 onward, the portions of these analyses for 70°–90°N are replaced with those of the Arctic Ocean Buoy Program (e.g., Thorndike and Colony, 1980). A linear smoother was applied to the transition zone 65°-75°N to incorporate the buoy pressure analyses into the composite pressure grids. The monthly surface air temperature grids from the University of East Anglia (Jones et al., 1986) are used to obtain daily values by cubic spline interpolation. The daily radiative forcing is computed from (6) and (7); a spatially invariant relative humidity of 90% is

used to obtain the vapor pressure in (6). The ocean dynamic topography and hence the ocean currents are temporally invariant, while the prescribed monthly rates of snowfall are climatological and spatially invariant. The spatially invariant vertical flux of oceanic heat into the mixed layer varies over the range 0–5 W m^{-2} in the sensitivity experiments of Section 3. Although the model contains a mixed layer in which the temperature varies spatially and temporally (when ice is not present), there is no horizontal heat transport by the ocean currents. As noted in previous studies (Walsh et al., 1985; Walsh and Zwally, 1990), the absence of ocean heat transport results in an over-simulation of ice extent during the winter. However, we use the ice model in this uncoupled state because (1) we wish to illustrate the multivariate sensitivity analysis procedure without the complications introduced by coupling, and (2) our examination of the simulated variations of ice thickness will focus on the Arctic Ocean.

The primary sea ice simulation (Section 5) begins on 1 January 1960 and continues through 1988. The model is initialized by an 8-year spin-up using the forcing data of 1960–1963, repeated twice. The sensitivity experiments of Section 4 use as their initial state the primary simulation's fields of ice thickness, concentration and velocity on 1 January 1980. This starting date was chosen for no other reason except that the simulations would span the years in which the Arctic buoy sea level pressure analyses were incorporated into the forcing data.

3. Statistical Model and Experimental Design

As the summary of the formulation in Section 2 suggests, the ice model results are potentially sensitive to many parameters in the ice physics and in the formulation of the atmospheric forcing. Because the sensitivity tests require simulations of about five years in order to determine the equilibrium response to a parameter variation, it can be prohibitively expensive to evaluate the interdependencies of the sensitivities for a complete span of the parameter space. (For example, sampling five values of each of only five parameters would require $5^5 = 3125$ simulations of about five years each.) Based on a methodology for design and analysis of computer experiments described by Sacks, Schiller, and Welch (1989), Sacks, Welch, Mitchell, and Wynn (1989), and

Welch et al. (1992), Bowman et al. (1992) have recently presented a prototype study of a method for the efficient testing of sensitivities in multi-dimensional parameter space. This method, which is similar to kriging in the spatial analysis literature, fits a statistical model to the output of a set of runs of a numerical model (see Appendix for details). The model response, evaluated in terms of certain metrics or integrated features of the output, is regarded as the dependent variable, while the model parameters are treated as independent variables. The statistical model postulates that a response is a realization of a stochastic process; the joint distribution of the statistical model response depends on several constants, which are fit to the data by using a maximum likelihood method. The accuracy of the statistical model is measured by cross-validation. The statistical model is a continuous function of the d parameters to which the sensitivities are to be evaluated, so the model is equivalent to an d-dimensional surface. This surface indicates the parameters and corresponding subranges to which the model output is most sensitive.

The sets of input data points (i.e., the values of the parameters) are obtained by Latin hypercube sampling (McKay et al., 1979). Given an experimental design in which the number of experiments is n, the input range for each parameter is divided into n equally-spaced values. For each experiment, the value of each input parameter is chosen randomly from the equally-spaced values without repeating previous values. (In the case of P^*, the values were equally spaced on a logarithmic scale.) The resulting set of parameter combinations spans the range of all the individual parameters and distributes the combinations throughout the parameter space. As noted above, the use of a complete regular grid of parameters is infeasible even in spaces of moderate dimension (5–10).

Iman and Conover (1982) described how to transform a random Latin hypercube into one with a desired correlation pattern. By iterating their procedure, near-zero correlations can be achieved between all pairs of input parameters. This controls the two-dimensional distributions of points better than a random Latin hypercube.

The number of runs necessary to produce a satisfactory statistical model is difficult to predict a priori. It depends in large part on the smoothness of the model response throughout the parameter space of interest. Experience suggests that a number equal to ten times the number of

important input factors is a good initial guess. The adaptive and sequential nature of the method is valuable in this regard, since additional runs can be added and the improvement in the statistical model gauged.

The specific assumptions we make typically endow the data with a Gaussian distribution in many dimensions. The likelihood or joint distribution of the data under this specification will depend on several constants. By using the maximum likelihood method to fit the constants of the statistical model to the data for a particular response, y, we specify the statistical model sufficiently to predict y by $\hat{y}$. For deterministic numerical models, the statistical model we use insists that $\hat{y}$ be an interpolator. Thus the model reproduces the output data directly at the input points.

As described by Wahba and Wendelberger (1980) in the context of spatial interpolation, the cross-validation method used for measuring accuracy proceeds as follows. An experimental run is set aside and a statistical model is fit to the remaining data. This model is then used to estimate the response at the set-aside point, and a comparison is made between the predicted and actual outcomes produced by the numerical model. The process is repeated for each combination of input parameter values, and the results are used to obtain an overall measure of accuracy.

On the basis of the sea ice model formulation in Section 2 and our previous experience with the model, thirteen parameters were chosen as independent variables to be input to the statistical model. Table 1 lists these variables, together with the range of values over which each was varied. These ranges should be kept in mind when interpreting the results: sensitivity with respect to a parameter would tend to decrease if a narrower range is chosen. The first three entries in Table 1 pertain to the model dynamics. C_a and C_w determine the strength of the air and water stress for given values of the wind and ocean currents (relative to the ice). An increase of P^* effectively hardens the ice and tends to reduce the ice motion when the ice is compact. Table 1's fourth entry, the minimum lead fraction, affects both the ice dynamics (through A and P^*) and the thermodynamics (through the albedo and the surface energy budget). In simpler formulations of sea ice, the minimum lead fraction is indeed a high-leverage parameter (Ledley, 1991a). Items 5–7 in Table 1 are the prescribed albedos for each of the three surface types; the ranges of these

quantities have been chosen to include the observational uncertainties in each. Items 8 and 9, the surface exchange coefficients, determine the magnitudes of the sensible and latent heat exchanges. One might expect Item 10, the snowfall rate, to be associated with competing effects. An increase of the snowfall rate favors thicker ice through the increase of the spring-summer albedo, while it favors thinner ice through the more effective insulation of the ice during winter. In Ledley's (1991b) energy balance model results, the net effect of increased snowfall is a decrease of annual mean ice thickness. Items 11 and 12 are crude parametric measures of cloud-radiative interactions. An increase of β decreases the depletion of the solar beam by cloudiness, thus increasing the incoming solar flux, F_s, at the surface. An increase of γ increases the downcoming longwave flux, F_ℓ, in direct proportion to the cloud fraction. Finally, an increase of the oceanic heat flux (Item 13) will tend to decrease the ice thickness by favoring ice ablation (or retarding ice accretion) on the underside of the ice.

Four measures of the ice response (the "y" of the Appendix) were explored in the sensitivity analysis. These were (a) the annual mean ice mass, (b) the annual mean ice-covered area, (c) the annual mean ice drift speed (averaged over all grid points containing ice) and (d) the annual range of ice-covered area, i.e., the difference between the maximum and minimum ice covered area during the year. In all four cases, the response was evaluated from the model output for the fourth year of a four-year simulation beginning on 1 January 1980.

4. Results of Sensitivity Analysis

Of an initial set of 81 randomly generated experiments, 70 were executed to completion. The remaining 11 experiments became numerically unstable. Furthermore, one of the stable cases gave a very extreme value for annual mean ice drift speed and was deleted for all responses. Statistical models were fitted, one for each response, using the remaining 69 good runs, but cross-validation accuracy appeared inadequate. Thus, a set of additional experiments was obtained by searching the original Latin hypercube design for the 50 largest holes in the input parameter space. The points defining the centers of these data-void regions of parameter space were then used to increase the

resolution of the analysis. Of the 50 additional simulations, 12 became numerically unstable prior to completion. Accuracy was judged to be inadequate still, and another 60 runs were chosen in the same way. Of these, another 10 were unstable, giving a total of 157 good runs from the three stages. The statistical models fitted to the aggregate data still have mixed degrees of accuracy. Figure 2 shows the cross-validation predictions versus the true (simulated) values. It can be seen that mass is fairly well predicted, except for one very discrepant case. Allowing the simulation to extend four more days proved this case to be unstable as well. Area is also reasonably well approximated by its statistical model, but drift speed and range of area are clearly inaccurate. Moreover, further data from the second and third-stage experimental designs did not appreciably improve the approximations for drift speed and range of area. We speculate below that the numerical model may be erratic in some regions of the parameter space, and hence unpredictable to some extent. In any case, collecting further data (at considerable computational cost) appears to have questionable marginal utility. Given the inaccuracy of the velocity and range-of-area models, the results below for these responses should be treated with caution. Results for the more useful mass and area responses appear to be fairly reliable, however. Inspection of the output data reveals no obvious anomalies. We note, however, that the mass data and drift speed data each vary over 1-2 orders of magnitude, whereas area and range-of-area show less variability. In this sense, mass and drift speed are more sensitive responses. We now ascribe these sensitivities to specific input parameters.

The important estimated single-parameter sensitivities are shown in Figure 3. These are obtained from the statistical predictor by integrating $\hat{y}$ with respect to all input parameters with one exception; i.e., integrating out all but one parameter and hence isolating its effect. For unimportant inputs these plots would be fairly horizontal, thus they are omitted. Table 2 quantifies the sensitivities by apportioning the total variability of each response to the various input parameters. For example, we see from Figure 3 that MLF and D1 have large effects on ice mass, and Table 2 shows that these two inputs indeed account for an estimated 37.4% and 34.5%, respectively, of the total variability in ice mass.

Such a decomposition of a response's variability amongst individual parameters is only valid if the response function is approximately additive in functions of single input parameters, over the ranges examined. As outlined in Appendix A, however, we can also identify joint effects of several inputs together. Such higher-order effects appear to be important only for ice mass. We now consider each response in detail.

4.1 Ice mass

As already noted, ice mass depends strongly on two inputs--MLF and D1. An increase of D_1 increases the rate of heat loss from the ice surface during the non-summer months, thereby increasing the conductive heat loss from the subsurface ice/ocean and increasing the freezing rate. A larger MLF increases the cold-season loss of sensible heat from the surface of each grid cell by allowing a larger area of direct contact between cold surface air and the relatively warm underlying ocean. These two variables work in tandem to modify the surface energy balance in the ice model: the effect of an increase of the MLF is greater if the sensible heat transfer coefficient is large, and an increase of the sensible heat transfer coefficient has a greater impact when the MLF is large. Figure 4a illustrates the effect of this two-parameter interaction by showing the total ice mass as a joint function of D_1 and MLF. Although not shown explicitly in Table 2, over 9% of the variance of the statistical model's response is explained by the interaction between these two parameters, over and above their individual additive effects.

4.2 Ice area

Approximately one half of the variance of the ice-area response is determined by the value of D_1 , the sensible heat exchange coefficient (Table 2, column 2). The physical mechanism in this case entails a more rapid loss of heat by the ocean and thus a more rapid cooling to freezing. Some ocean areas that would not cool to freezing with a small value of D_1 will do so as D_1 becomes large. Similarly, the tendency for ice to be thicker when D_1 is larger will result in a longer ice season at most grid points, thus increasing the ice-covered area over time. Table 2 shows that D_2 ,

the turbulent exchange coefficient for latent heat, also contributes to the ice-area response, although to a lesser extent than D_1 . Physically, greater rates of evaporation (larger D_2) will increase the rate of heat loss by the surface, thereby enhancing the likelihood that the temperature will drop to freezing in regions equatorward of the ice boundary.

4.3 Mean Drift Speed

As Table 2 and the above discussion indicate, the ice mass and ice area generally depend more strongly on parameters in the thermodynamic formulation than on the parameters in the ice dynamics formulation. The dependences of the mean drift speed are quite different. Table 2 shows that the drift speed is determined primarily by the atmospheric and oceanic drag coefficients and secondarily by the ice strength parameter and the minimum lead fraction. The effects of the surface winds on the ice motion are well known, and in this analysis the atmospheric drag coefficient is the primary contributor to the response of the ice drift speed. As the atmospheric drag coefficient is increased, the model's average ice drift speed increases. In contrast, the sensitivity analysis shows that the average ice drift speeds decrease with increasing values of the oceanic drag coefficient. Thus the ocean currents tend to impose a drag on the ice from beneath the ice, slowing the motion forced by the surface winds from above the ice.

Figure 4b shows the competing effects on ice drift speeds of the drag forces at the top and bottom surfaces of the ice. The effects are clearly interdependent. For example, in the absence of oceanic drag, the mean drift speed increases substantially (more than three-fold) as the atmospheric drag coefficient increases from 0 to .0015. Similarly, the tendency for the oceanic drag coefficient to decrease the ice drift speed is much greater when the atmospheric drag coefficient is larger.

4.4 Ice range-of-area

As indicated in Table 2, no single parameter dominates the response of the range-of-area (winter to summer). The percentages of explained variance are spread over more of the input parameters than in the case of the other response variables. The larger influences do, however, generally come from the parameters that influence the ice dynamics (i.e., C_a, C_w, p* and MLF).

The interdependencies among these sensitivities are again quite strong. Figure 4c, for example, shows that the range-of-area depends on the atmospheric and oceanic drag coefficients in a way that is qualitatively similar to the corresponding dependencies of the ice drift speed (Figure 4b). To the extent that the ice velocities determine the range-of-area (by expanding the winter ice coverage through horizontal transport), the interdependencies in Figure 4c are quite plausible.

The interplay between the ice strength and the atmospheric drag coefficient (C_a) is shown in Figure 3d in terms of the response of the range-of-area. The interdependence is quite strong and systematic in this case. The dependence on ice strength increases from negligible at small values of C_a to quite strong at large values of C_a. This dependence is also quite plausible if winter ice coverage is enhanced by advective transport, since ice strength should have a greater impact on ice transport when the air stress (the primary motive force) is large.

4.5 Numerical model diagnostics

Almost 20% of the ice model simulations were numerically unstable and therefore did not contribute a model response at certain input points. Analysis of the locations of these input configurations, combined with examination of the statistical model to highlight regions where prediction is apparently difficult, shed some light on the reliability of the numerical model.

The plots in Figure 5 show the relationship between the statistical model cross-validation residuals or errors, as given by equation (A.10), and the input parameters. For example, Figure 5a plots the cross-validation errors for ice mass versus oceanic drag. Large statistical-model errors, including the extreme error already noted in Section 3, tend to occur when oceanic drag is low. The dots plotted along the bottom of this figure indicate the values of oceanic drag for the 34 unstable runs. This shows that unstable runs also tend to occur when oceanic drag is low.

Inspection of the analogous plots for the other inputs and outputs shows:

- Atmospheric Drag tends to be high for the unstable runs.
- The five biggest absolute errors for the ice-area statistical model all occur when the sensible heat flux is very close to its lower limit (Figure 5b).

- Mean drift speed and range-of-area are inaccurately predicted when the oceanic drag coefficient is low.

Inaccuracy of a statistical model could imply inadequacy of the modelling strategy. There is some overlap, however, between regions where errors are large and those where the numerical model is demonstrably unstable. Thus, we suspect that the responses are inherently difficult to predict when the oceanic drag coefficient is low and/or atmospheric drag coefficient is high.

Further evidence that the response functions can be erratic (hence difficult to predict) stems from the following investigation. In an attempt to describe the behavior of the ice model as it approaches an unstable region of the parameter space, we performed a set of 16 experiments in which simulations were executed at points along a line connecting the center of the parameter space to a point found to lie within an unstable region. The unstable point chosen was located at an extreme of the ranges chosen for both the atmospheric and the oceanic drag coefficients. The model response for simulations 1–12 varied smoothly and predictably as the input parameters progressed away from the center of the parameter space. Simulations 13, 15 and 16 were found to be numerically unstable. The model response for simulation 14, however, appeared to fall somewhat in line with those for 1–12. Thus it appears that there may be points in the domain which could appear to have a stable model response but, in fact, lie within an unstable region of the model parameter space. Due to the nonlinearity of the model and the relatively short simulation length (4 years), it is apparent that some simulations initialized with points found within an unstable region of the parameter space may not reveal themselves as such. These points may contribute to the noise that is apparent in some of the statistical model results, e.g., Figure 4b.

The examples discussed above indicate that the statistical methodology is able to capture the fundamental physical sensitivities and their interdependencies. In general, the interdependencies are most apparent and most plausible in the sensitivities to the dynamical parameters. This tendency may be a consequence of the fact that the ice model generally contains more sophisticated (and presumably more realistic) formulations of the ice dynamics than of the thermodynamics. Conclusions about the generality of our findings must therefore await applications to more

comprehensive formulations of sea ice thermodynamics and the corresponding forcing (e.g., Curry and Ebert, 1992).

5. Results of Multidecadal (1960–1988) Simulation

The multidecadal simulation, which was intended to provide a framework for an examination of the temporal variability, used the parameter values listed in the right hand column of Table 1. All parameter values are from within the ranges used for the sensitivity tests of Section 4. While we did not use the sensitivity analysis to choose these parameter values (the multidecadal simulation was performed prior to the sensitivity tests), the sensitivity analysis provides an excellent tool for determining the subset of combinations of parameter values that will result in a certain equilibrium. This combination of parameters produced a model climatology that, in some respects, compares favorably with observational data, especially in the Arctic Ocean (see results presented below). In other respects, especially in the peripheral seas during winter, the model's climatology is biased with respect to observational data. The most notable bias, the excessive sea ice extent during winter, is consistent with the absence of ocean dynamics and the corresponding horizontal transport of oceanic heat.

Figure 6 shows the model's seasonal climatologies of ice thickness and velocity. Characteristic features are the clockwise gyre of ice motion in the Arctic Basin, the relatively strong velocities advecting ice through Fram Strait and into the Greenland Sea, and the thickness build-up offshore of northern Greenland and the Canadian Archipelago. Annual mean ice thicknesses range from 2–3 meters in the Alaskan Arctic and the Siberian shelves to 5–6 meters north of Greenland and Baffin Island. Ice extent during the winter and spring is excessive in the North Atlantic and the Bering Sea for the reason noted above.

On shorter timescales, the model velocities show considerably more variability than can be deduced from Figure 6. Figure 7 shows the trajectories during 1987 of simulated buoys placed on the ice initially (January 1, 1987) at the locations of actual buoys monitored monthly by the Arctic Ocean Buoy Program (Colony and Rigor, 1991). The simulated trajectories, based on the daily velocities of the ice model, are superimposed on the ice thicknesses and multiyear ice

concentrations for December 31, 1987. In most cases, the trajectories of the simulated buoys correspond well to the actual month-to-month buoy displacements (Figure 8), in terms of the net displacements and the meanders over monthly-to-seasonal timescales. Two buoys are not well simulated: the motion of the buoy that exits the Arctic through Fram Strait is undersimulated, suggesting an underestimate of the current-induced component of the motion; and the simulated buoy near the center of the Beaufort Gyre undergoes a small displacement toward the west rather than to the north. The motion of the buoys in the Chukchi and Lincoln Seas are reproduced especially well by the model.

Figure 7a also shows that the simulated ice thickness for December, 1987, is quite similar to the model's winter climatological field (Figure 6a). The spatial pattern of the multiyear ice concentration (Figure 7b) closely resembles the pattern of ice thickness, indicating that the age of the ice is a key determinant of spatial variations of ice thickness. An unrealistic feature of the multiyear ice distribution in Figure 7b is the region of thick multiyear ice along the Siberian coast in the western Chukchi Sea. The westward wind stress in this region results in an excessive build-up of sea ice to thicknesses such that the ice does not melt completely during the summer. By definition, the surviving ice becomes multiyear ice. While such build-ups do not occur in all years, they occur in a sufficient number of years that they produce noticeable features in the seasonal mean plots of Figure 6. The excessive component of this build-up appears to result from a variety of reasons. The coarse resolution of the model domain results in coastal grid points which have some edges perpendicular to the mean drift pattern of ice in this region. Convergence of ice against these unrealistic coastal edges may cause the model-derived ice thicknesses to be larger than observed. Also, the model seems to provide an inadequate representation of the northerly surface ocean currents and poleward heat treansport through Bering Strait. For longer timescales, this may also contribute to the excessive build-up of ice in this region.

The annual net ice growth simulated by the model is shown in Figure 9. Because the ice is advected horizontally by the ice motion, the location in which a sample of ice melts is generally different from the location in which it originally formed by freezing. The prevailing pattern of ice drift in Figure 6 is such that the continental shelves of central Asia and the eastern Beaufort Sea are

regions of net ice formation. The regions into which ice advection occurs (e.g., the Greenland Sea, the Barents Sea) are regions of net ice melt (negative annual ice growth). This effect of ice transport is equivalent to a flux of freshwater or, alternatively, a flux of salinity from the regions of net ice melt to the regions of net ice formation. Figure 9 shows that much of the central Arctic Ocean is characterized by net annual ice growth of 0.4–0.6 m in the model simulation; this ice generally forms in areas of ice divergence during the cold season, and the net growth is offset by advection into the regions of ice melt. Figure 9 also contains several examples of more localized "conveyor belts" indicative of advection from a zone of ice formation to a zone of ice melt in peripheral seas: the Bering Sea, Baffin Bay and Hudson Bay. An unrealistic feature of Figure 9 is the net annual ice growth to the west and south of Spitsbergen. The absence of horizontal heat transport by the ocean into this region results in a situation in which subfreezing water temperatures are maintained erroneously as ice is advected southwestward from Spitsbergen.

In order to address the timescales of the fluctuations of ice thickness, we have evaluated anomalies of the simulated ice thickness along a transect that generally parallels the long-term pattern of ice drift from the Beaufort Sea into and along the Transpolar Drift Stream (Figure 1). The anomalies are the departures from the model's monthly means. As shown in Figure 10, the anomalies of ice thickness are characterized by timescales of several seasons to several years. When measured along the transect (left-right in Figure 10), the horizontal scales of the anomalies are typically several hundred to a thousand km. There is some evidence of advection of the anomalies by a long-term mean drift as the anomalies in various portions of Figure 10 tilt downward to the right. Anomalies for which this tilt is especially apparent occur in the early 1960s, the late 1970s – early 1980s, and the late 1980s. The positive anomaly that is northwest of Greenland in the late 1970s generally maintains its identity along the entire transect until its passage through Fram Strait in 1984.

An intriguing finding based on submarine data is the apparent decrease of ice thickness between 1976 and 1987 in the region east of northern Greenland (Wadhams, 1990). Although Wadhams' submarine data were from slightly different tracks and different calendar months (October 1976 and May 1987), the data indicate ". . . a significant decrease in mean ice thickness . . .. This thinning amounts to a loss of volume of at least 15% over an area of

300,000 km^2" (Wadhams, 1990, p. 795). A key issue pertaining to the differences between the two distributions of ice thickness is the representativeness of the "anomalies:" Do the differences represent interannual fluctuations or are they indicative of a more systematic trend? Wadhams' examination of buoy drift prior to May 1987 suggested that the former possibility is real.

In order to address both the spatial and temporal representativeness of the data samples compared by Wadhams, we have denoted by heavy dots in Figure 10 the space-time points corresponding to Wadhams' submarine data. The model-derived anomalies are strongly positive in October 1976 and nearly zero in May 1987. In this respect the anomalies are consistent with the findings of Wadhams (1990). However, the anomalies of these two years are not representative of a systematic trend in the model results. In the Fram Strait area, the model-derived thickness anomalies were preceded and followed by anomalies of a different sign. The overall pattern of ice thickness anomalies (Figure 10) shows a weak tendency toward thicker ice during the 30 years beginning in 1960. However, this trend is not statistically significant and is due primarily to the preponderance of negative anomalies in the middle and late 1960s. It is noteworthy in this regard that there is only modest evidence in Figure 10 of the heavy ice conditions associated with the "Great Salinity Anomaly" of the late 1960s and early 1970s (Dickson et al., 1988). The simulated ice was slightly thicker than "normal" in Fram Strait during 1970–1972, but an upstream signal is not apparent in Figure 10. The absence of such a signal may not be surprising because the observational evidence of the Great Salinity Anomaly comes from the waters well to the south of Fram Strait. Moreover, the effects of salinity are not included in this formulation of the model. The model-derived outflow of ice through Fram Strait is nevertheless larger during 1970–1971 than at any other time during the simulation, but the earliest oceanographic indications of the Great Salinity Anomaly appeared several years earlier (Dickson et al., 1988).

As a further indication of the absence of any significant negative trends in the model output, Figure 11 shows the time series of simulated (total) ice-covered area as well as the simulated (total) ice mass. The only apparent indication of a negative trend is found in the wintertime maxima of ice-covered area, which decrease by approximately 5% from the mid-1970s to the mid-1980s.

This decrease of wintertime areal coverage is consistent with that obtained from satellite passive microwave imagery for 1978–1987 (Gloersen and Campbell, 1991). However, any claims concerning temporal trends in the model output must be qualified in several respects. First, the parameters of the ice model can easily be adjusted to produce a trend of either sign in the simulated ice mass or ice coverage. The long-term (1960–1988) simulation was indeed tuned to give a temporally stable time series by varying the cloud depletion parameter β (Table 1). Similar tuning could have been performed with many of the other parameters in Table 1, as well as with parameters not included in Table 1. Second, as described below, the correlations between simulated and observed variations of ice coverage are such that much of the observed variance is unexplained by the model. It is therefore quite difficult to regard as meaningful the secular trends representing only small portions of the variance of the simulated time series.

Figure 12 is a time-longitude representation of the simulated anomalies of ice-covered area. While this figure is intended to permit a comparison of the timescales of anomalies of ice-covered area and ice thickness (Figure 10), the horizontal axis is longitude in Figure 12 rather than distance along a central Arctic "transect" as in Figure 10. These two figures nevertheless indicate that the timescales of ice-area anomalies are much shorter than those of ice thickness. Most anomalies of the simulated ice coverage at a particular longitude last less than a year, and there is no indication of a systematic tendency for east-west advection of the anomalies. In these two respects, the contrast with the thickness anomalies in Figure 10 is striking. The simulated fluctuations of ice-covered area are more rapid than those derived from observational data (Chapman and Walsh, 1992, Fig. 5), which show the persistence of some relatively large anomalies over timescales of several years. The period of the Great Salinity Anomaly noted earlier is one such example. The absence of oceanic coupling appears to contribute to the rapidity of the simulated fluctuations of ice-covered area, since the model is effectively missing a slowly varying source of temperature and salinity anomalies that directly affect the expansion and contraction of the sea ice margin.

Figure 13 shows the correlations between the simulated and observed anomalies of ice-covered area in 20° sectors of longitude. (The correlations are limited to the 1972–1988 period of homogeneously charted ice concentrations from the U.S. Navy/NOAA Joint Ice Center.) While

the correlations vary considerably with longitude, they are generally largest ($\gtrsim 0.7$) in the Bering Sea, the eastern Canadian waters, and in the sectors of several of the North Atlantic subpolar seas. The smallest correlations (110°E, 110–150°W) are found in sectors in which the advance of the ice is land-blocked during much of the year. The average of the correlation over all sectors is only 0.53. Although deficiencies in the observational data may account for some unexplained variance, it is apparent that much of the observed variability is not captured by the model. Fleming and Semtner (1991) have shown that oceanic coupling can result in a modest increase of explained variance over interannual timescales, but even coupled models have yet to reproduce more than half the interannual variance of corresponding time series of observed ice coverage. This "state of the art" implies that ice models must be used with extreme caution in applications pertaining to trend detection.

6. Conclusion

The findings obtained here may be viewed in several lights. On the one hand, the statistical model results show that the ice model sensitivities are many and that the sensitivities to various parameters are interdependent. The sensitivities and their many interdependencies are quantifiable, as shown in Section 4. However, the complex set of sensitivities casts a pervasive shadow over the interpretation of sea ice simulations driven by interannually variable forcing, since the model response to the variable forcing may change considerably if the model parameters are changed. On the other hand, the simulation described in Section 5 was able to produce interannual variations consistent with the ice thickness data of Wadhams (1990) and the ice-extent variations reported by Gloersen and Campbell (1991). If these correspondences are valid, the model results then imply that interannual variability is a major contributor to the changes of ice thickness and extent over timescales of a decade or less. The multidecadal model results also indicate that the timescales of ice thickness anomalies are much longer than those of ice-extent anomalies, suggesting that ice thickness is a much more conservative variable on a year-to-year basis. If the actual ice-ocean system varies similarly, then the sampling requirements for the monitoring of ice thickness may be less severe than those for areal ice coverage. Hypotheses such as this one should be pursued

through further experiments with models containing more realistic forcing (e.g., radiative fluxes) and physics (e.g., oceanic coupling).

With regard to the physical-statistical methodology examined in Sections 3 and 4, the ultimate value of such an approach may lie in its quantitative depiction of the sensitivities relative to the observational uncertainties in the various parameters and combinations thereof. In the case of the minimum lead fraction, for example, the total ice mass varies by nearly a factor of two as the minimum lead fraction varies from 1% to 4%, which is arguably the range of observational uncertainty of the minimum lead fraction in the wintertime Arctic. When the sensitivity analysis procedure is extended to coupled models driven with more realistic thermodynamic forcing, the results may provide an indication of the priorities for the narrowing of observational uncertainties in the various parameters.

Acknowledgements. This work was supported by NOAA's Office of Global Programs through Grant COM NA16RCO520-01, NASA's Interdisciplinary Research Program through Grant IDP-88-009, the NSERC of Canada, and AFOSR and NSF through Grant NSF-DMS-9121554. Computer time was provided by Cray Research and the National Center for Supercomputing Applications, which is sponsored by the National Science Foundation. We thank Norene McGhiey for typing the manuscript.

7. References

Bowman, K. P., J. Sacks and Y.-F. Chang, On the design and analysis of numerical experiments, J. Atmos. Sci., 49, in press, 1992.

Chapman, W. L., and J. E. Walsh, Recent variations of sea ice and air temperature in high latitudes, Bull. Amer. Meteor. Soc., 73, in press, 1992.

Colony, R. L., and I. Rigor, Arctic Ocean Buoy Program Data Report for 1 January 1987 – 31 December 1987, Tech. Memor. APL-UW TM7-91, 152 pp., Applied Physics Laboratory, Univ. Washington, Seattle, 1991.

Curry, J. A., and E. E. Ebert, Annual cycle of radiation fluxes over the Arctic Ocean: Sensitivity to cloud optical properties, J. Climate, 5, in press, 1992.

Dickson, R. R., J. Meincke, S.-A. Malmberg and A. J. Lee, The "Great Salinity Anomaly" in the northern North Atlantic, 1968–1982, Progr. Oceanogr., 20, 103–151, 1988.

Fleming, G. H., and A. J. Semtner, Jr., A numerical study of interannual ocean forcing on arctic sea ice, J. Geophys. Res., 96, 4589–4603, 1991.

Gloersen, P., and W. J. Campbell, Recent variations in Arctic and Antarctic sea ice cover, Nature, 352, 33–36, 1991.

Hibler, W. D., III, A dynamic thermodynamic sea ice model, J. Phys. Oceanogr., 9, 815–846, 1979.

Idso, S. B., and R. D. Jackson, Thermal radiation from the atmosphere, J. Geophys. Res., 74, 5397–5403, 1969.

Jones, P. D., S. C. B. Raper, R. S. Bradley, H. F. Diaz, P. M. Kelly and T. M. L. Wigley, Northern Hemisphere surface air temperature variations, 1851–1984, J. Clim. Appl. Meteor., 25, 161–179, 1986.

Ledley, T. S., The climatic response to meridional sea ice transport, J. Climate, 4, 147–163, 1991a.

Ledley, T. S., Snow on sea ice: Competing effects in shaping climate, J. Geophys. Res., 96, 17,195–17,208, 1991b.

McKay, M. D., W. J. Conover and R. J. Beckman, A comparison of three methods for selecting values of input variables in the analysis of output from a computer code, Technometrics, 21, 239–245, 1979.

Parkinson, C. L., and W. M. Washington, A large-scale numerical model of sea ice, J. Geophys. Res., 84, 311–337, 1979.

Preller, R. H., and P. G. Posey, The Polar Ice Prediction System—A sea ice forecasting system, Rep. 212, 42 pp., Nav. Ocean Res. and Dev. Agency, Stennis Space Center, MS, 1989.

Riedlinger, S. H., and R. H. Preller, The development of a coupled ice-ocean model for forecasting ice conditions in the Arctic, J. Geophys. Res., 96, 16,955–16,977, 1991.

Ross, B., and J. E. Walsh, A comparison of simulated and observed fluctuations in summertime arctic surface albedo, J. Geophys. Res., 92, 13,115–13,125, 1987.

Sacks, J., Schiller, S.B., and Welch, W.J. (1989). Designs for Computer Experiments. Technometrics, 31, 41-47.

Sacks, J., Welch, W.J., Mitchell, T.J., and Wynn, H.P. (1989). Design and Analysis of Computer Experiments (With Discussion). Statistical Science, 4, 409-435.

Thorndike, A. S., and R. Colony, Arctic Ocean Buoy Program Data Report: 19 January 1979 – 31 December 1979, 131 pp., Polar Science Center, Univ. Washington, Seattle, 1980.

Wadhams, P., Evidence for thinning of the Arctic ice cover north of Greenland, Nature, 345, 795–797, 1990.

Wahba, G., and J. Wendelberger, Some new mathematical methods for variational objective analysis using splines and cross validation, Mon. Wea. Rev., 108, 1122–1143, 1980.

Walsh, J. E., W. D. Hibler III and B. Ross, Numerical simulation of Northern Hemisphere sea ice variability, 1951–1980, J. Geophys. Res., 90, 4847–4865, 1985.

Walsh, J. E., and H. J. Zwally, Multiyear sea ice in the Arctic: Model- and satellite-derived, J. Geophys. Res., 95, 11,613–11,628, 1990.

Welch, W.J., Buck, R.J., Sacks, J., Wynn, H.P., Mitchell, T.J., and Morris, M.D. (1992). Screening, Predicting, and Computer Experiments. Technometrics, 34, 15-25.

Zillman, J. W., A study of some aspects of the radiation and heat budgets of the southern hemisphere oceans, Meteorological Study No. 26, Bureau of Meteorology, Dept. of the Interior, Canberra, Australia, 562 pp, 1972.

Appendix

The essence of the formulation of the statistical model is summarized here; details and generalizations are given by Sacks, Welch, Mitchell, and Wynn (1989).

Consider the stochastic model

$$y(\mathbf{x}) = \beta + Z(\mathbf{x}) \tag{A.1}$$

where $Z(\mathbf{x})$ is a random function, β is a constant, and y is the response. For two sets of inputs $\mathbf{x}$ and $\mathbf{w}$, the covariance between $Z(\mathbf{x})$ and $Z(\mathbf{w})$ is

$$\mathrm{Cov}\left(Z(\mathbf{x}), Z(\mathbf{w})\right) = \sigma^2 R(\mathbf{x}, \mathbf{w}) , \tag{A.2}$$

where σ^2 is a (variance) constant and $R(\mathbf{x}, \mathbf{w})$ is a correlation function assumed to be from the family

$$R(\mathbf{x}, \mathbf{w}) = \prod_i \exp\left(-\theta_i \left| x_i - w_i \right|^{p_i}\right) . \tag{A.3}$$

The unknown constants θ_i , p_i , β, σ^2 are to be estimated as described below. The power p_i , which is constrained to lie in the interval $1 \le p_i \le 2$, determines the shape of the correlation function in the i'th dimension of the parameter space; while $1/\theta_i$ is the effective length scale of the correlation in the i'th dimension of the parameter space. With this correlation structure, two points $\mathbf{x}$ and $\mathbf{w}$ that are close together will have highly correlated y's. This property is exploited to develop a predictor.

Let $\mathbf{y} = (y_1, ..., y_n)$ denote the observed performances at an experimental design of n input vectors, $\mathbf{s}_1, ..., \mathbf{s}_n$, and

$$\mathbf{r}_\mathbf{x} = \left[R\left(\mathbf{x}, \mathbf{s}_k\right) \right], \mathbf{R} = \left[R\left(\mathbf{s}_k, \mathbf{s}_{k'}\right) \right] , \tag{A.4}$$

Then $\mathbf{r}_\mathbf{x}$, which is an $n \times 1$ vector, is the correlation between the point $\mathbf{x}$ and all of the sample points, $\mathbf{s}_k$, while $\mathbf{R}$, which is an $n \times n$ matrix, is the correlation between all possible pairs of sample points. It can be shown that the best linear predictor of $y(\mathbf{x})$ at an untried input point $\mathbf{x}$ is

$$\hat{y}(x) = \hat{\beta} + \mathbf{r}_{x'}\mathbf{R}^{-1}(\mathbf{y} - \hat{\beta}\,\mathbf{1}) , \tag{A.5}$$

where

$$\hat{\beta} = (\mathbf{1}'\mathbf{R}^{-1}\mathbf{1})^{-1}\mathbf{1}'\mathbf{R}^{-1}\mathbf{y} \tag{A.6}$$

and $\mathbf{1}$ is an n-vector of 1's.

To compute these predictions and their mean-squared errors, the correlation parameters θ_i and p_i in (A.2), β in (A.1), and σ^2 must be estimated. Because the predictor is an interpolator, it produces a surface that passes through all the data points for any feasible choice of θ_i , p_i , β, and σ^2; this can be shown to follow from (A.5) and (A.6). We select θ_i , p_i , β, and σ^2 to give an optimal fit to the data in the sense of maximizing the likelihood L. Assuming that $\mathbf{y}$ has a normal distribution, the likelihood to be maximized is

$$L(\theta, \mathbf{p}, \beta, \sigma^2) = \frac{1}{(2\pi)^{n/2}(\sigma^2)^{n/2}(\det \mathbf{R})^{1/2}} \exp\left(-\frac{1}{2\sigma^2}(\mathbf{y} - \beta\,\mathbf{1})'\mathbf{R}^{-1}(\mathbf{y} - \beta\,\mathbf{1})\right) . \tag{A.7}$$

For given θ_i and p_i , it is possible to determine the values of β and σ^2 maximizing the likelihood. The optimization therefore reduces to numerical maximization of

$$-n \log(\hat{\sigma}^2) - \log(\det \mathbf{R}) , \tag{A.8}$$

where

$$\hat{\sigma}^2 = \frac{1}{n}(\mathbf{y} - \hat{\beta}\,\mathbf{1})'\mathbf{R}^{-1}(\mathbf{y} - \hat{\beta}\,\mathbf{1}) , \tag{A.9}$$

and $\hat{\beta}$ is given by (A.6).

Accuracy of a statistical model can be assessed through cross validation. At design point x_i , we predict the observed response y_i via (A.5) using all the data <u>except</u> observation i. In the plots of Figure 5, $\hat{y}_{-i(x_i)}$ is plotted against y_i for i = 1 , . . ., n. The cross validation residuals or errors on the vertical axes of the plots in Figure 5 are given by

$$y_i - y_{-i(x_i)} . \tag{A.10}$$

To estimate the dependence of a response on input parameter j we integrate out all the other inputs from $\hat{y}$:

$$\mu_{j(x_j)} = \int \hat{y}(x_1, \ldots, x_{13}) \prod_{i \neq j} (dx_i) / \prod_{i \neq j} (b_i - a_i),$$

where $[a_i, b_i]$ is the range of values for x_i. These are plotted versus x_j in Figure 3.

Similarly, the dependence on the joint effect of x_j and x_k can be estimated by integrating out all variables except these two,

$$\mu_{jk(x_j, x_k)} = \int \hat{y}(x_1, \ldots, x_{13}) \prod_{i \neq j,k} dx_i / \prod_{i \neq j,k} (b_i - a_i),$$

and so on for higher-order effects. These two-dimensional effects are plotted against x_j and x_k in the contour plots of Figure 4. To assess the importance of the joint effect over and above that explained by $\mu_{j(x_j)}$ and $\mu_{k(x_k)}$, we consider the estimated interaction effect

$$\mu_{jk(x_j, x_k)} - \mu_{j(x_j)} - \mu_{k(x_k)} + \mu_0,$$

where

$$\mu_0 = \int \hat{y}(x_1, \ldots, x_{13}) \prod_{i \neq j} dx_i / \prod_{i \neq j} (b_i - a_i),$$

is the overall estimated average value of the response y. If this interaction is small, x_j and x_k have approximately additive effects, it is sufficient to look at the separate $\mu_{j(x_j)}$ and $\mu_{k(x_k)}$ effects, and $\mu_{jk(x_j, x_k)}$ need not be inspected.

Table 1. Parameters varied in ice model sensitivity analysis.

Variable	Symbol	Use in model formulation	Range	Value in primary simulation (1960–1989)
1. Atmospheric drag coefficient	C_a	Eq. (2): $\rho_a C_a \lvert \vec{V}_a \rvert$	0.0000–0.0017	0.0012
2. Oceanic drag coefficient	C_w	Eq. (3): $\rho_w C_w \lvert \vec{V}_w \vec{V}_i \rvert$	0.0–10.0	5.5
3. Ice strength parameter	P^*	Eq. (4): $P = P^* h e^{-C(1-A)}$	2,750–275,000 N m^{-2} (logarithmic scale)	27,500 N m^{-2}
4. Minimum lead fraction	MLF	Imposed constraint: $A \leq (1 - MLF)$	0.00–0.06	0.015
5. Snow albedo	α_{snow}	Eq. (5): $(1 - \alpha_{snow}) F_s$	0.50–1.00	0.80
6. Ice albedo	α_{ice}	Eq. (5): $(1 - \alpha_{ice}) F_s$	0.30–0.80	0.65
7. Open water albedo	α_{water}	Eq. (5): $(1 - \alpha_{water}) F_s$	0.00–0.50	0.10
8. Exchange coefficient, sfc. sensible heat	D_1	Eq. (5): $D_1 \lvert \vec{V}_a \rvert (T_a - T_o)$	0.0–6.0	2.284
9. Exchange coefficient, sfc. latent heat	D_2	Eq. (5): $D_2 \lvert \vec{V}_a \rvert (q_a - q_o)$	0.1–1.2	1.0
10. Snowfall rate	SR	Eq. (5): Change of α, K	0.0–5.0 m yr^{-1}	0.41 m yr^{-1}
11. Cloud depletion of solar flux	β	Eq. (6): $1 - 0.6 C_f^{\beta}$	1.0–4.0	2.3
12. Cloud enhancement of longwave flux	γ	Eq. (7): $1 + \gamma C_f$	0.1–0.5	0.275
13. Oceanic heat flux	F_o	End of Section 2 (ice accretion/melt rate)	0.0–5.0 W m^{-2}	2.0 W m^{-2}

Input Parameter	Mass	Area	Velocity	Range
Atmospheric Drag Coefficient	0.0	1.1	38.6	16.6
Oceanic Drag Coefficient	0.1	4.0	32.4	9.4
Ice Strength	2.1	0.3	5.2	20.3
Minimum Lead Fraction	26.6	0.0	5.2	11.3
Snow Albedo	1.7	1.4	0.0	3.8
Ice Albedo	0.0	0.4	0.0	0.0
Open Water Albedo	0.0	0.0	0.0	1.2
Turbulent Exchange (Sensible Heat)	31.1	47.4	5.7	4.2
Turbulent Exchange (Latent Heat)	1.0	5.9	0.7	0.7
Snowfall Rate	0.0	0.0	0.0	7.0
Cloud Depletion (Shortwave Flux)	1.5	0.5	0.0	0.0
Cloud Depletion (Longwave Flux)	4.5	5.3	0.1	0.4
Oceanic Heat Flux	1.8	0.0	0.0	0.0

Table 2. Percent variance explained of four model responses by each single sensitivity parameter.

FIGURE CAPTIONS

Figure 1. The grid used for the ice model. Crosses denote transect along which ice thickness anomalies are evaluated in Section 5.

Figure 2. Cross-validation predictions versus true (simulated) values for the four model responses: (a) ice mass, (b) ice area, (c) mean ice drift speed, and (d) winter-summer range of area.

Figure 3. Examples of single-parameter sensitivities of ice model. Abscissa contains values of parameter, ordinate contains values of "response" variable.

Figure 4. Examples of joint (two-parameter) sensitivities of ice model. Contoured values are those of response variable identified above each plot; abscissa and ordinate contain values of parameters.

Figure 5. Examples of statistical model cross-validation residuals for (a) ice mass versus oceanic drag coefficient and (b) ice area versus sensible heat flux.

Figure 6. Seasonal mean ice velocity vectors and ice thicknesses for the simulation spanning 1960–1988. Seasons indicated in lower left portion of each panel are (a) winter (Jan–Mar), (b) spring (Apr–Jun), (c) summer (Jul–Sep) and (d) autumn (Oct–Dec).

Figure 7. Trajectories of simulated buoys for the period January 1–December 31, 1987. Heavy dots denote end of trajectory. Buoy trajectories are superimposed on fields of (a) ice thickness and (b) concentration of multiyear ice.

Figure 8. Monthly positions of arctic buoys during 1987. Heavy dots denote final positions (December 31, 1987). Buoys were deployed by Arctic Ocean Buoy Program (Colony and Rigor, 1991).

Figure 9. Annual net ice growth (m) in the model simulation of 1960–1988. Negative values denote annual net melt of ice.

Figure 10. Time evolution of simulated ice thickness anomalies along transect of Figure 1. (Right-hand portion of each panel is the Fram Strait/Greenland Sea area.) Anomalies are defined as the departures from the monthly means of the model results. Positive anomalies are blue and green, negative anomalies are red and yellow. Heavy dots

denote space/time points corresponding to Wadhams' (1990) submarine measurements.

Figure 11. Time series of simulated total ice-covered area and ice mass for the period 1960–1988.

Figure 12. Time-longitude sections of the simulated anomalies of ice-covered area. Anomalies are defined as the departures from the corresponding monthly means of the model results. Positive anomalies are blue and green, negative anomalies are red and yellow.

Figure 13. Correlations between simulated and observed anomalies of ice-covered area (1972–1988) in 20° sectors of longitude.

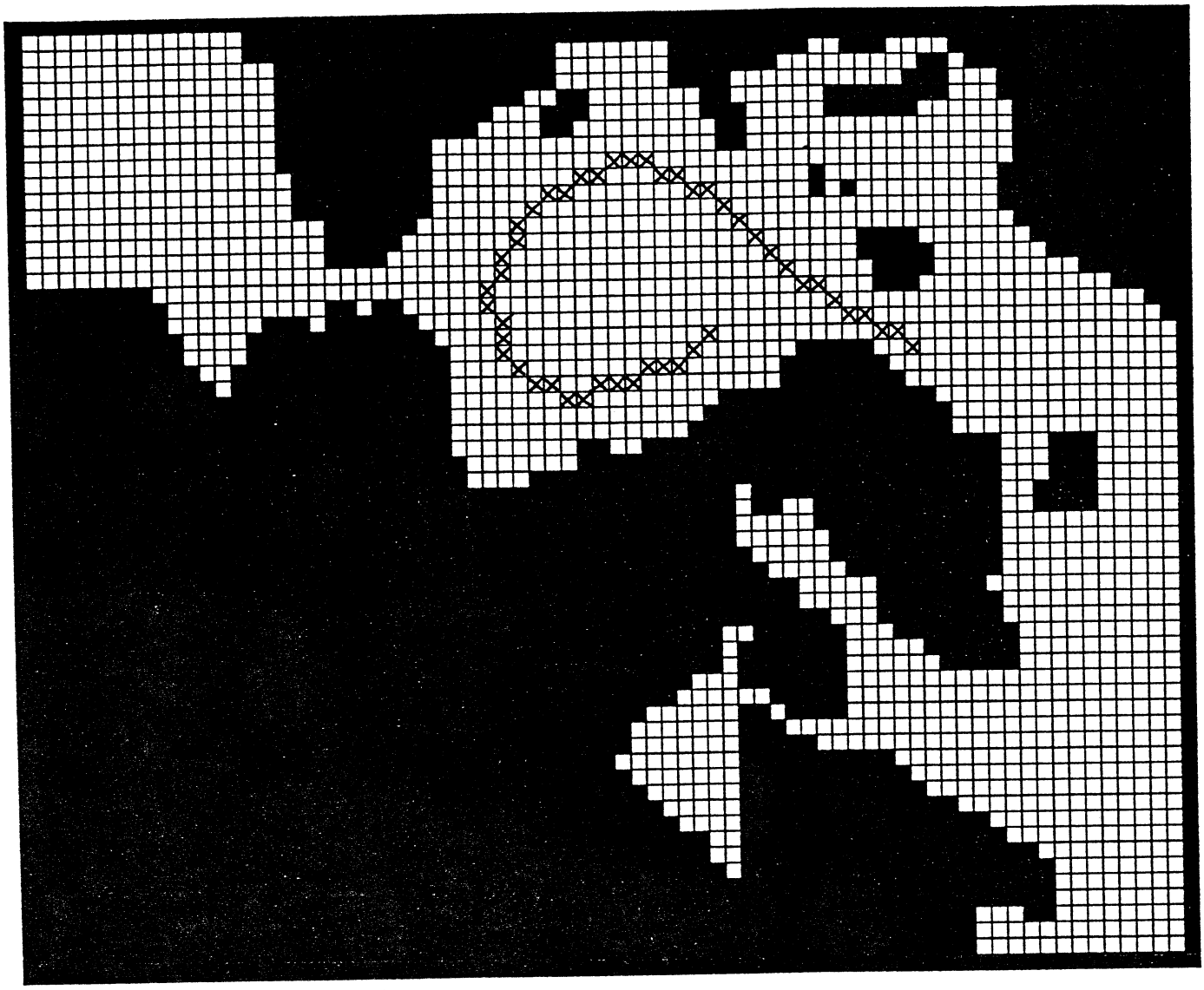

Figure 1. The grid used for the ice model. Crosses denote transect along which ice thickness anomalies are evaluated in Section 5.

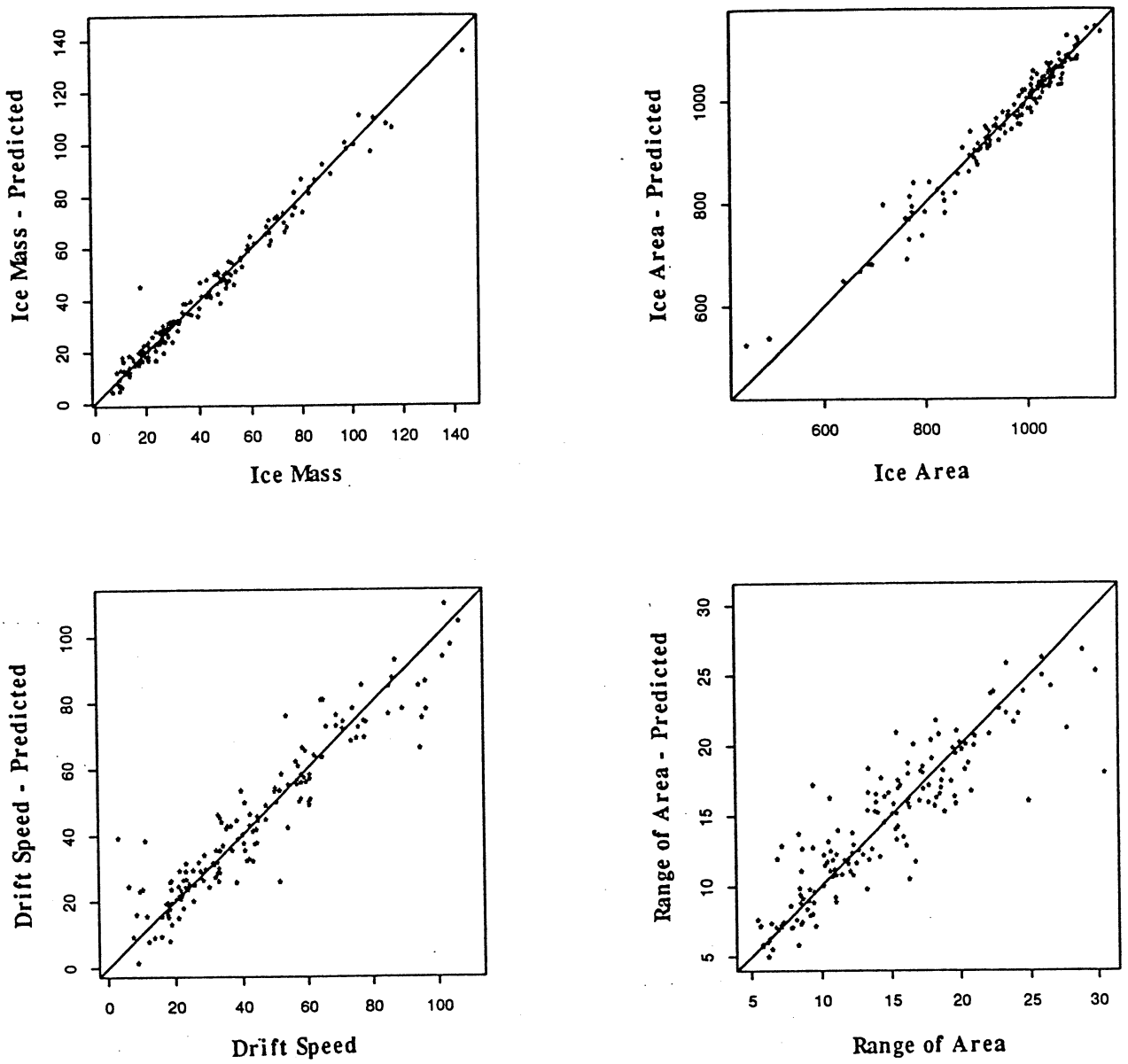

Figure 2. Cross-validation predictions versus true (simulated) values for the four model responses: (a) ice mass, (b) ice area, (c) mean ice drift speed, and (d) winter-summer range of area.

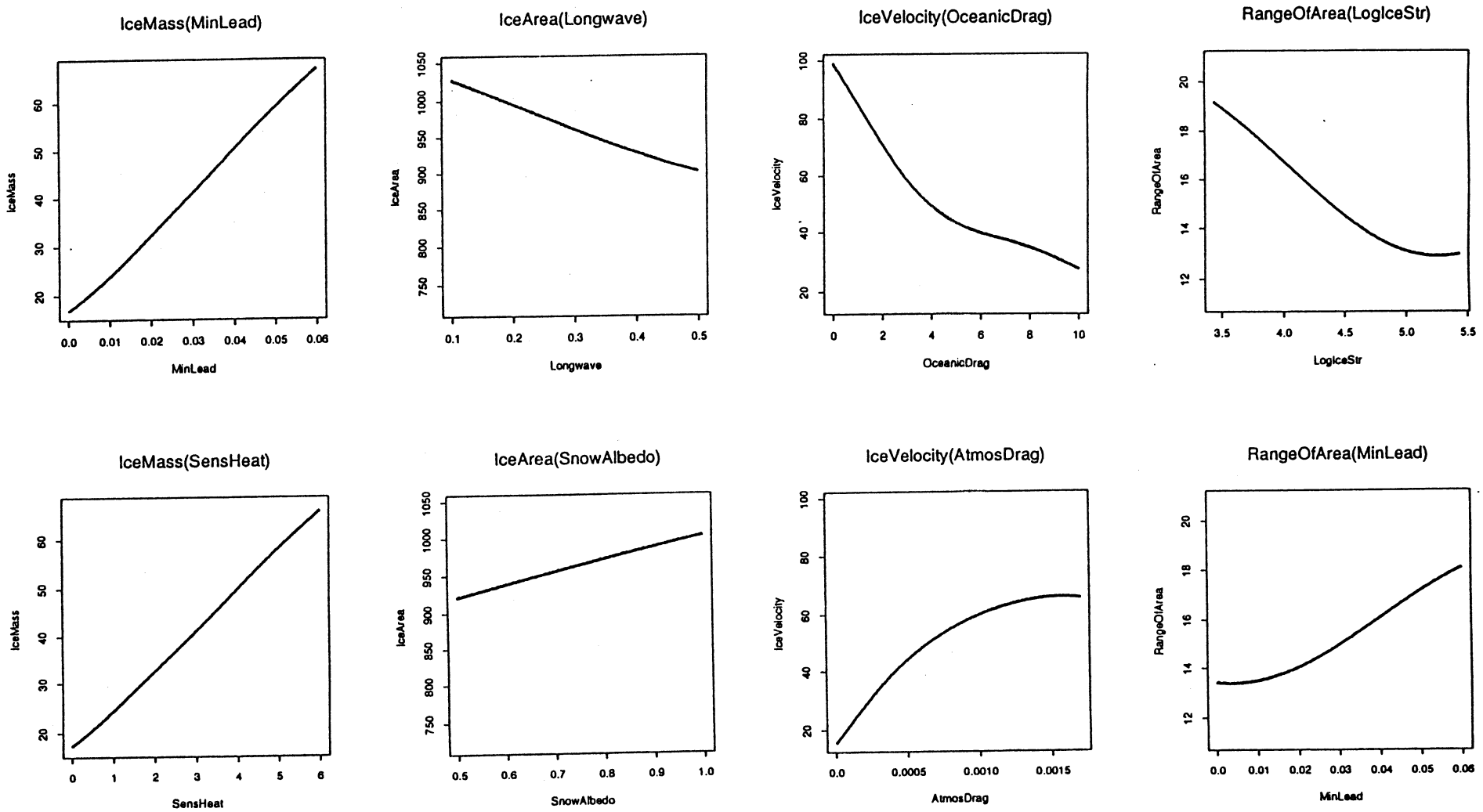

Figure 3. Examples of single-parameter sensitivities of ice model. Abscissa contains values of parameter, ordinate contains values of "response" variable.

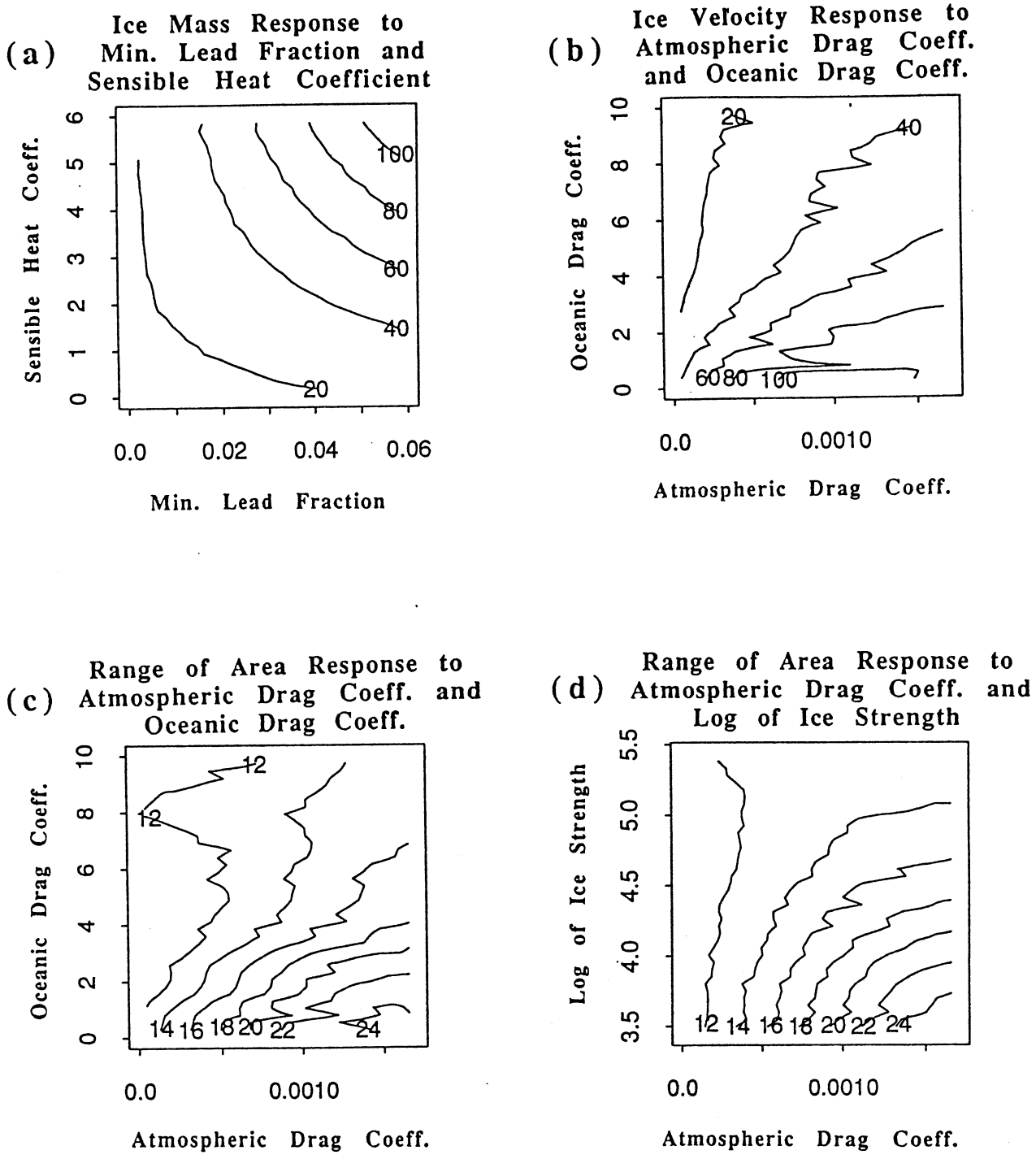

Figure 4. Examples of joint (two-parameter) sensitivities of ice model. Contoured values are those of the response variable identified above each plot; abscissa and ordinate contain values of parameters.

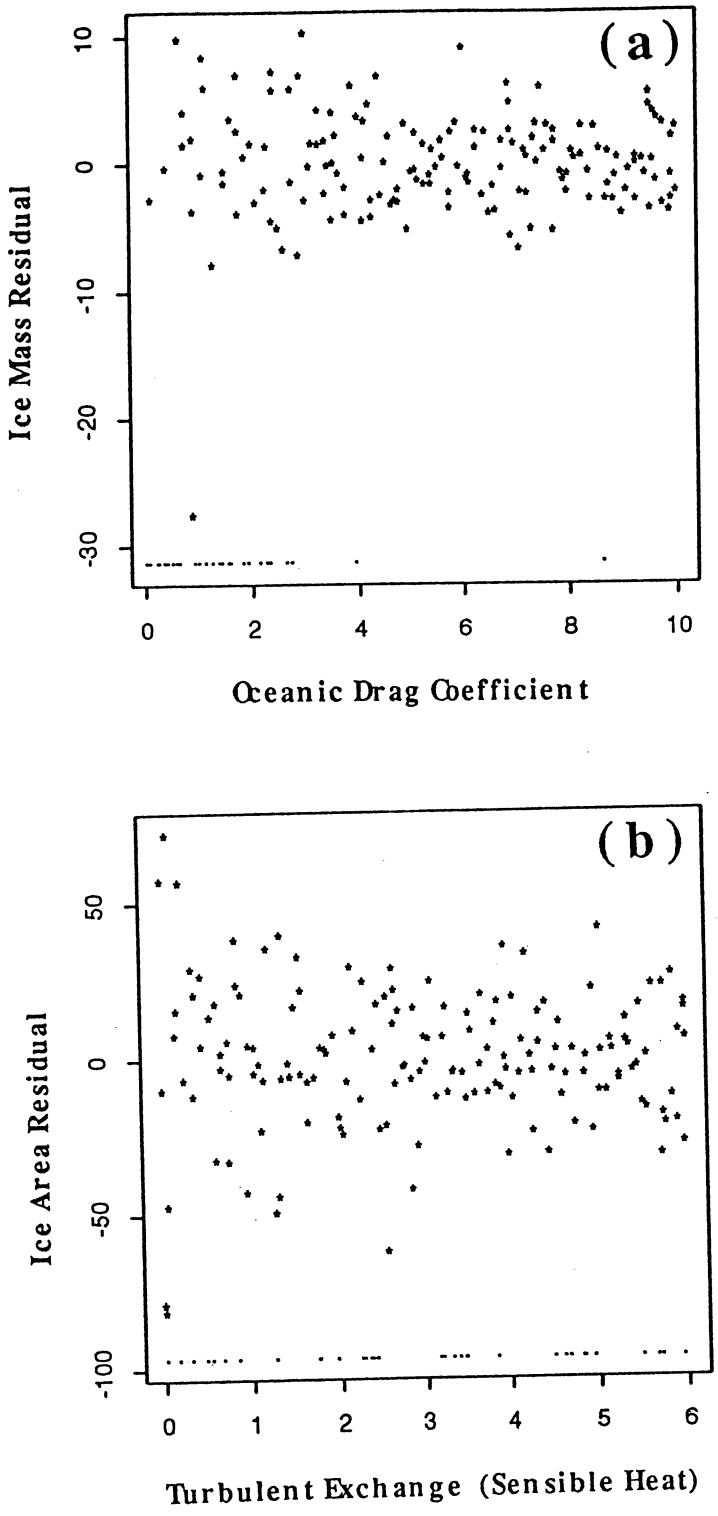

Figure 5. Examples of statistical model cross-validation residuals for (a) ice mass versus oceanic drag coefficient and (b) ice area versus sensible heat flux.

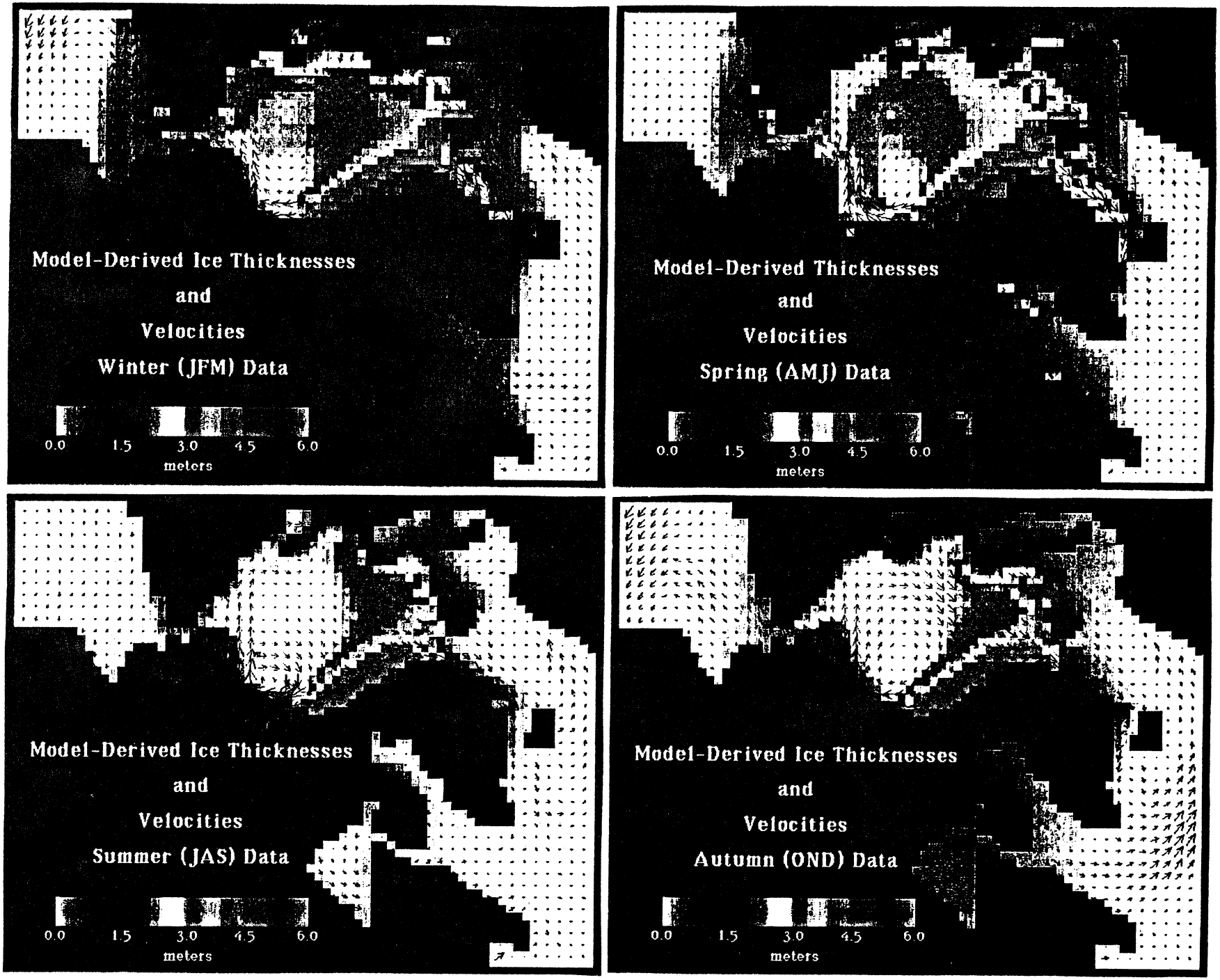

Figure 6. Seasonal mean ice velocity vectors and ice thicknesses for the simulation spanning 1960–1988. Seasons indicated in lower left portion of each panel are (a) winter (Jan–Mar), (b) spring (Apr–Jun), (c) summer (Jul–Sep) and (d) autumn (Oct–Dec).

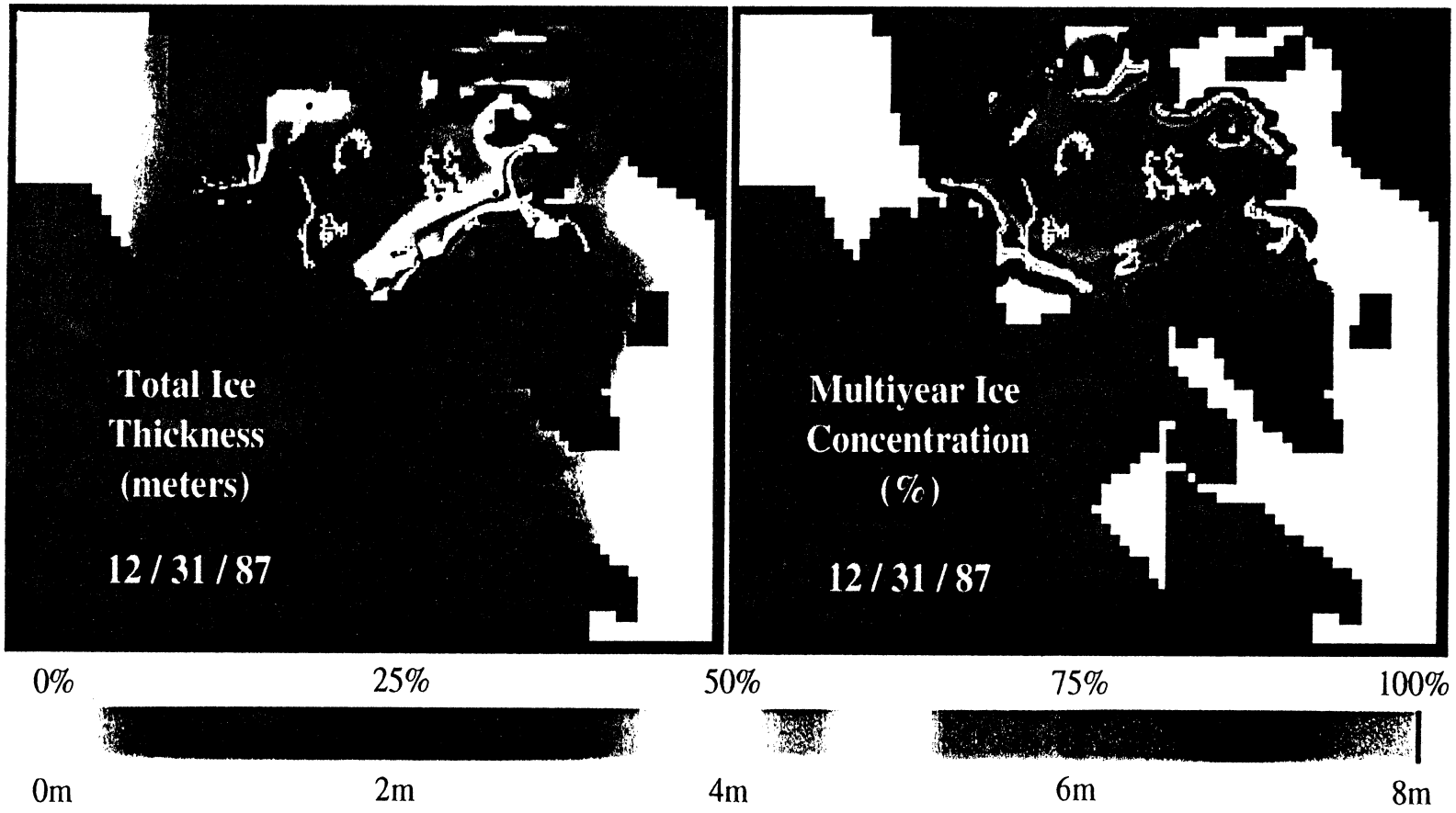

Figure 7. Trajectories of simulated buoys for the period January 1–December 31, 1987. Heavy dots denote end of trajectory. Buoy trajectories are superimposed on fields of (a) ice thickness and (b) concentration of multiyear ice.

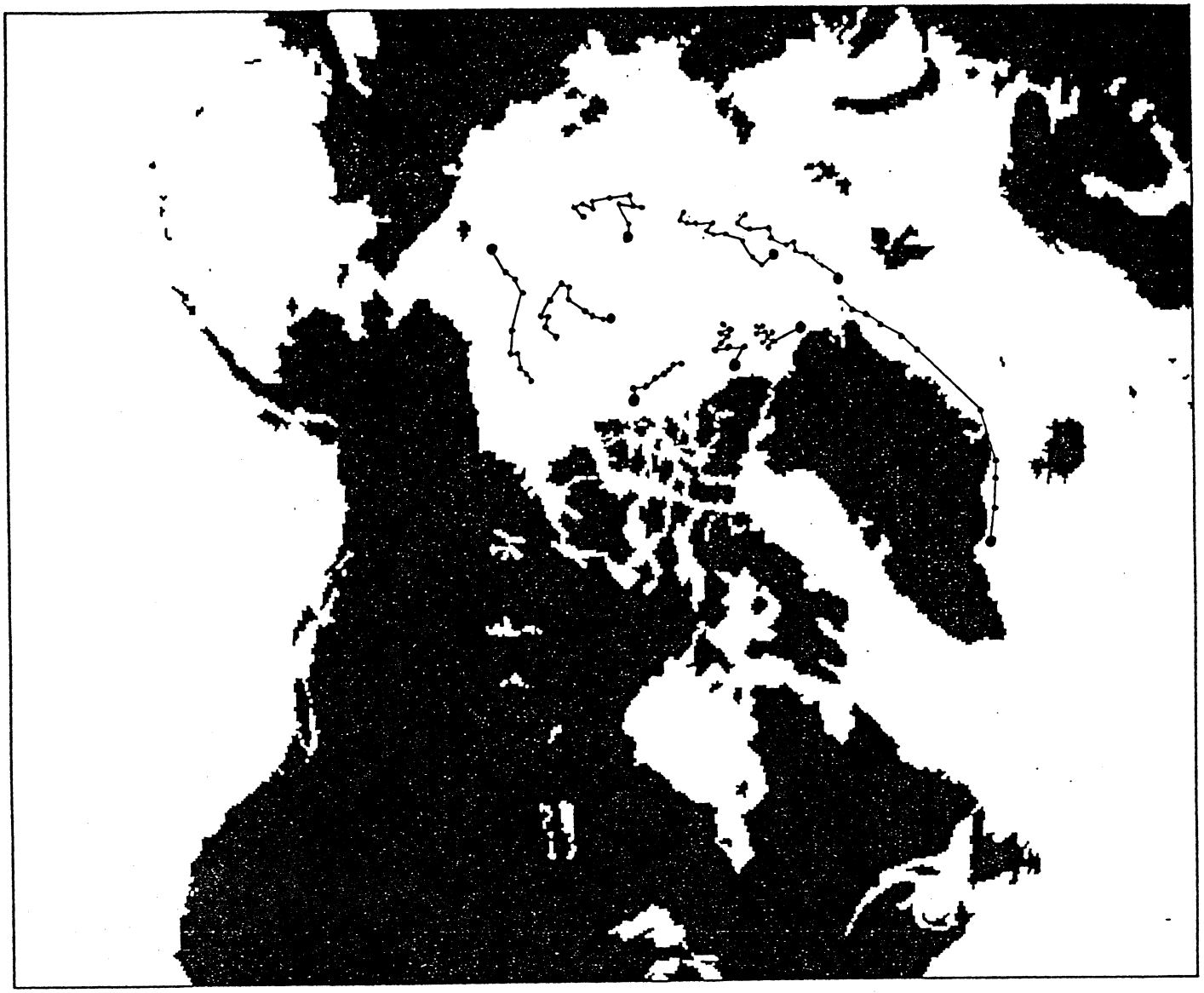

Figure 8. Monthly positions of arctic buoys during 1987. Heavy dots denote final positions (December 31, 1987). Buoys were deployed by Arctic Ocean Buoy Program (Colony and Rigor, 1991).

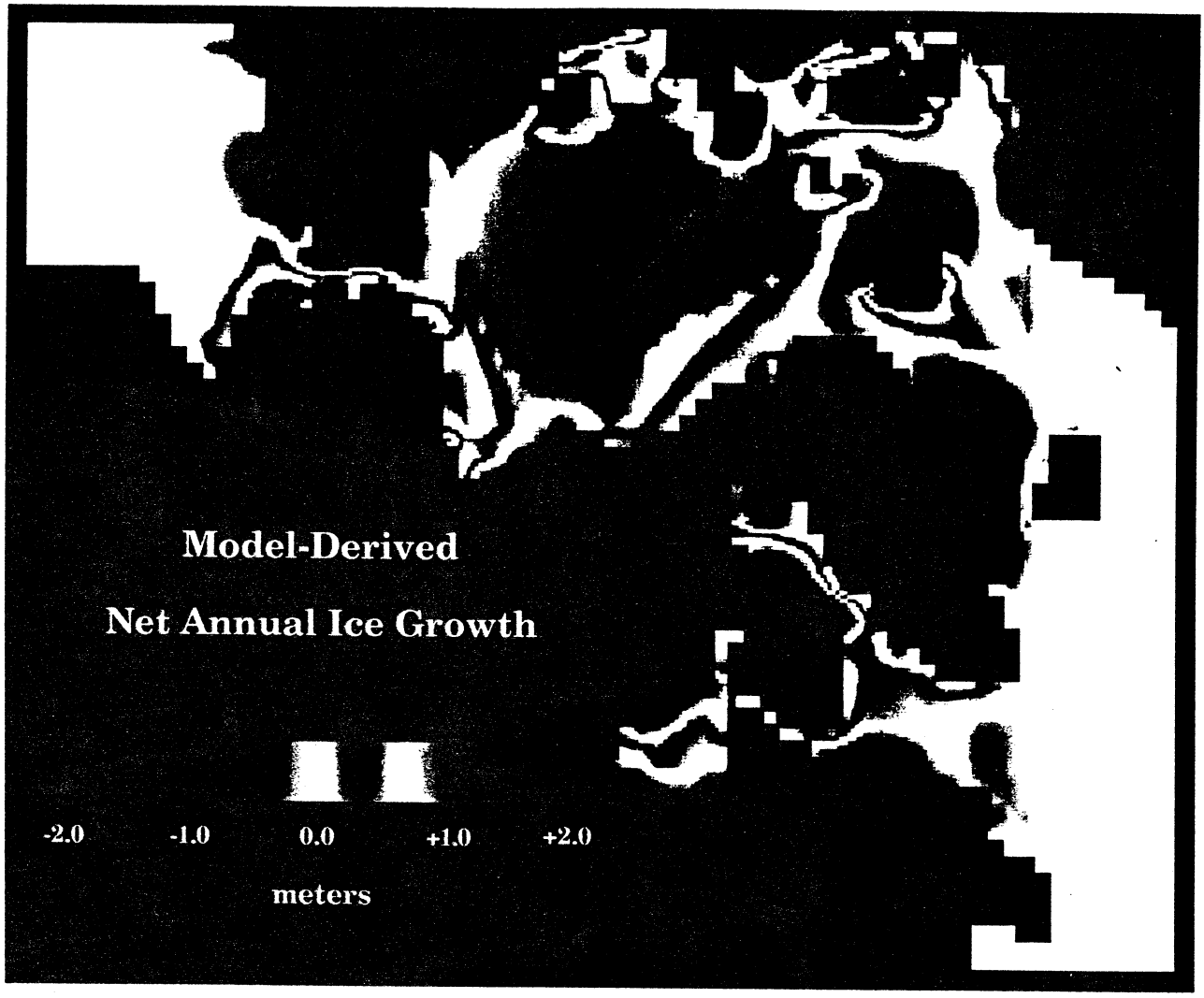

Figure 9. Annual net ice growth (m) in the model simulation of 1960–1988. Negative values denote annual net melt of ice.

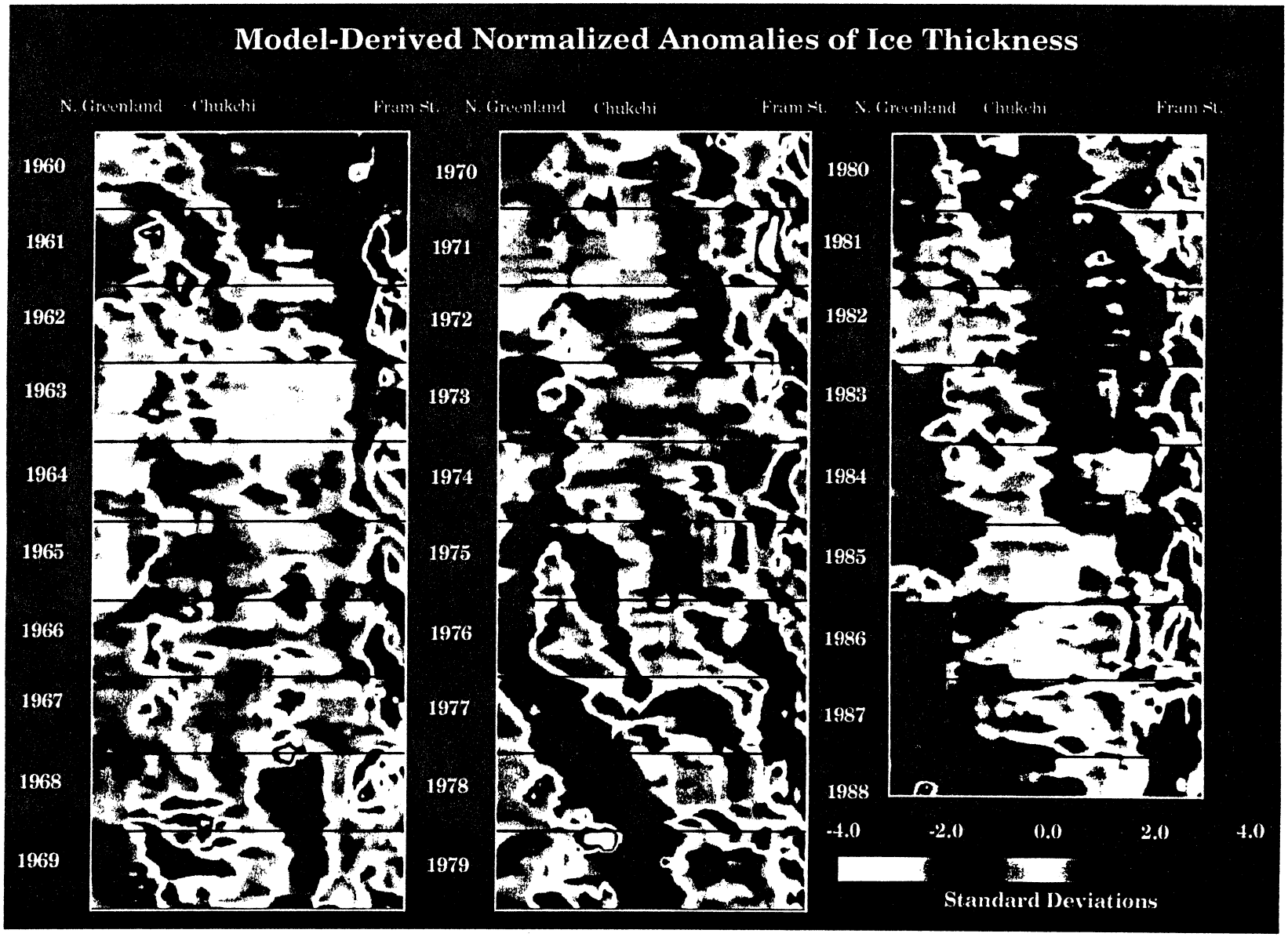

Figure 10. Time evolution of simulated ice thickness anomalies along transect of Figure 1. (Right-hand portion of each panel is the Fram Strait/Greenland Sea area.) Anomalies are defined as the departures from the monthly means of the model results. Positive anomalies are blue and green, negative anomalies are red and yellow. Heavy dots denote space/time points corresponding to Wadhams' (1990) submarine measurements.

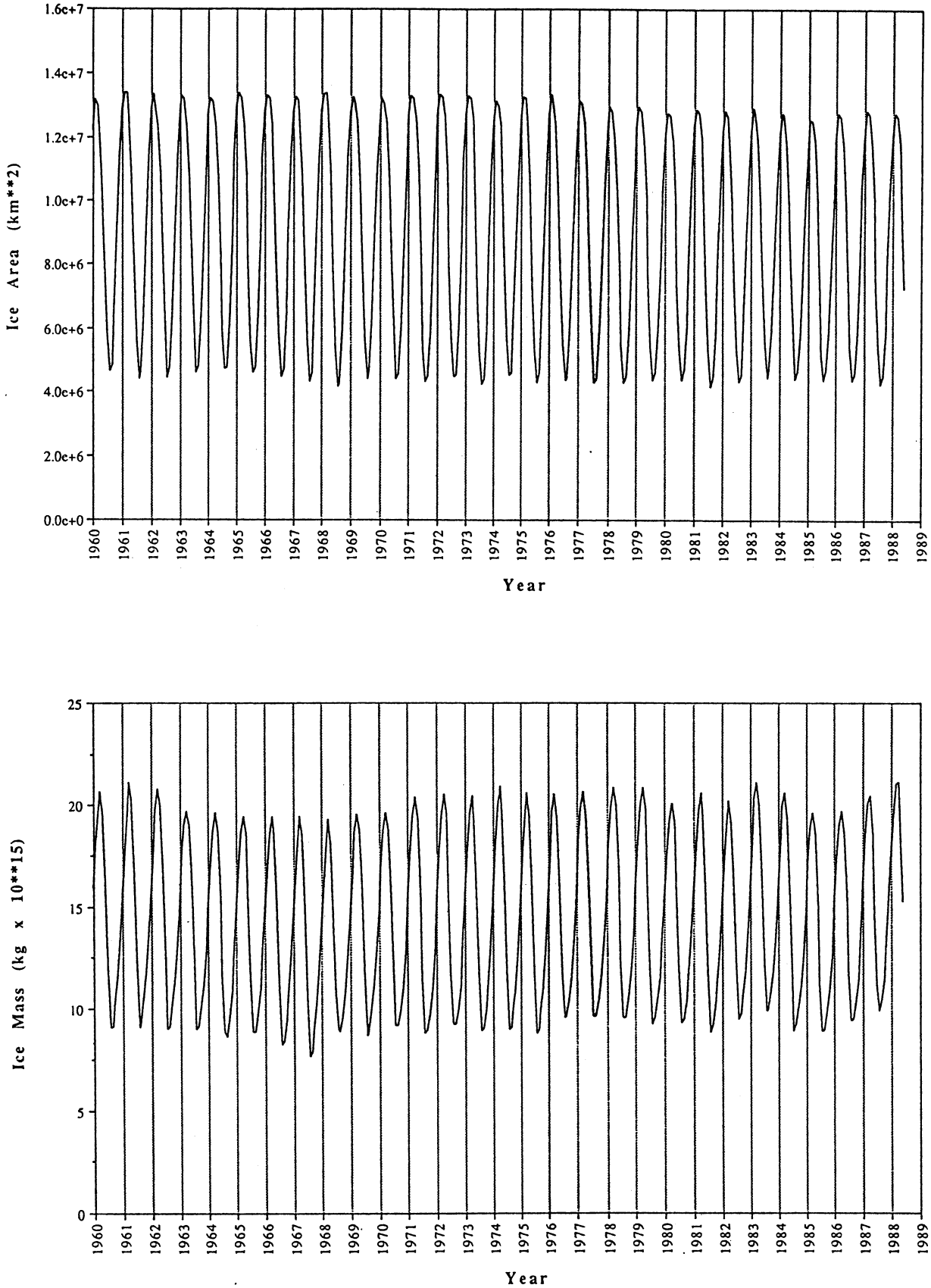

Figure 11. Time series of simulated total ice-covered area and ice mass for the period 1960–1988.

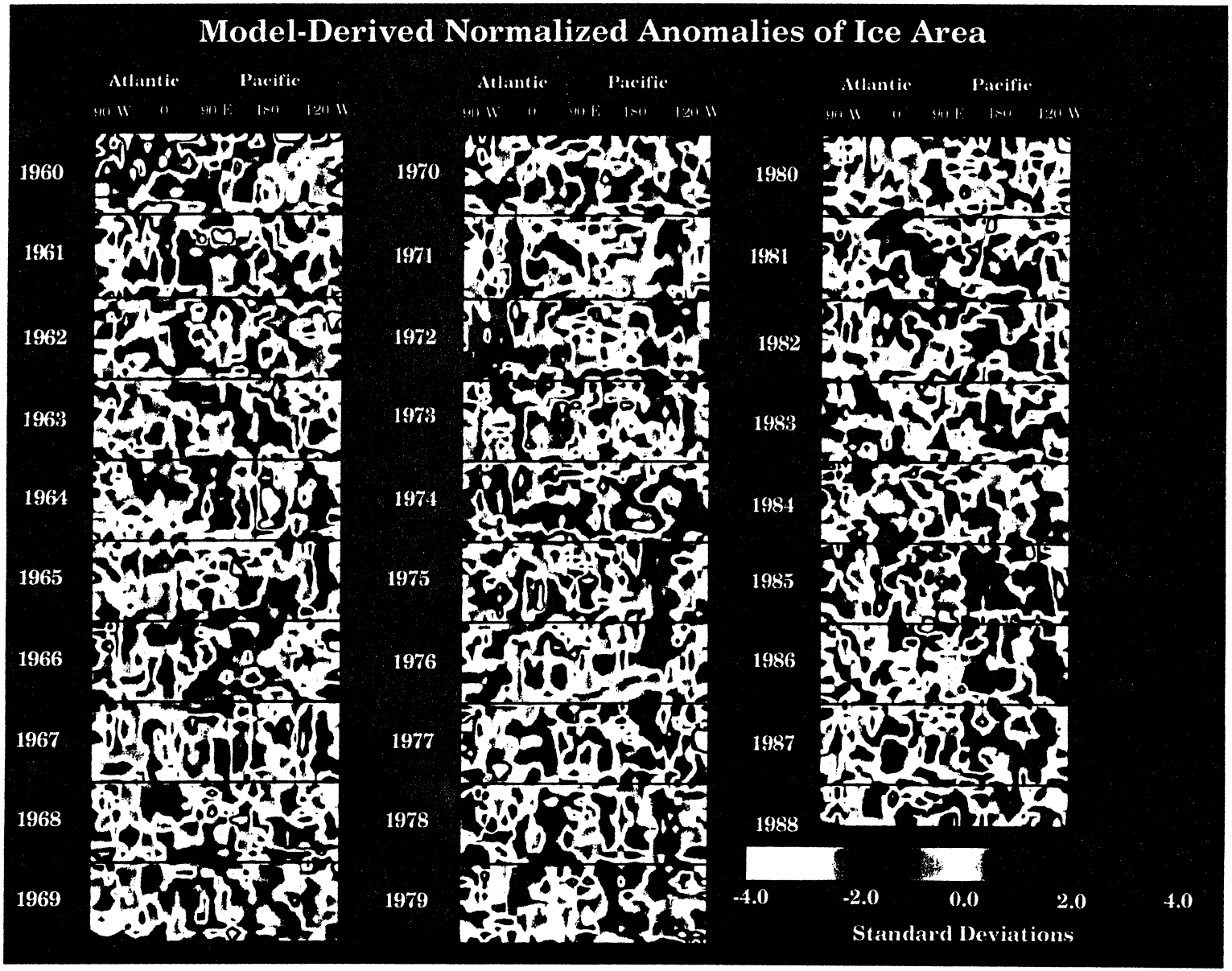

Figure 12. Time-longitude sections of the simulated anomalies of ice-covered area. Anomalies are defined as the departures from the corresponding monthly means of the model results. Positive anomalies are blue and green, negative anomalies are red and yellow.

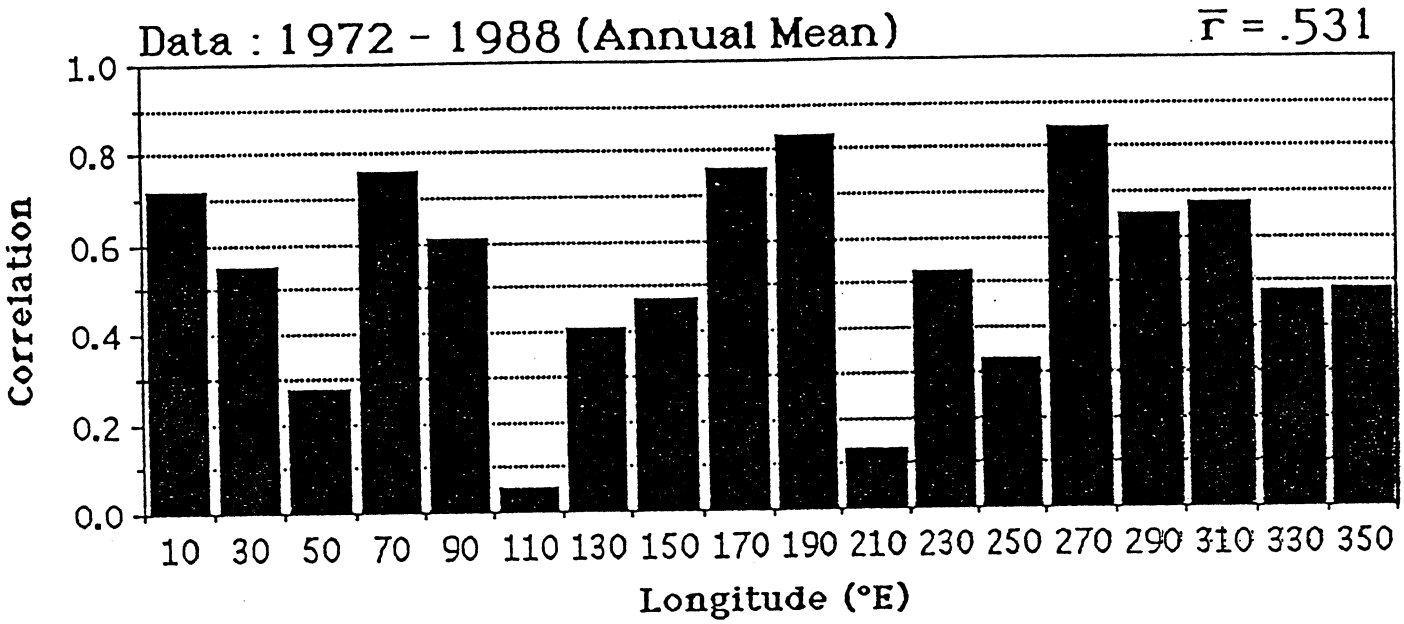

Figure 13. Correlations between simulated and observed anomalies of ice-covered area (1972–1988) in 20° sectors of longitude.